Nitrogen-doped Carbon Nanofibers on Expanded Graphite as Oxygen Reduction Electrocatalysts

Marthe E. M. Buan,[a] Navaneethan Muthuswamy,[a] John C. Walmsley,[b] De Chen[a] and Magnus Rønning*[a]

[a] Department of Chemical Engineering, Norwegian University of Science and Technology, 7491 Trondheim, Norway

[b] SINTEF Materials and Chemistry, Høgskoleringen 5, 7465 Trondheim, Norway

* Corresponding author. E-mail: magnus.ronning@ntnu.no

Abstract

A single-step chemical vapor deposition method using simple gaseous precursors was employed to grow nitrogen-doped carbon nanofibers from Fe and Ni particles on the surface of expanded graphite (N-CNF/EG). Due to the high electronic conductivity of the expanded graphite the N-CNF/EG could be used as electrocatalysts without the need for harsh purification procedures. Electrochemical testing showed that the N-CNFs grown from Fe exhibited a notable activity for the oxygen reduction in both acidic and alkaline electrolyte, in addition to demonstrating a high durability with a well-preserved catalytic activity after 1600 cycles in O_2-saturated 0.5M H_2SO_4. Physicochemical characterization revealed the formation of N-CNFs with a bamboo-like structure, encapsulated Fe particles and high pyridinic nitrogen content. The combination of high ORR-activity, an easily scalable synthesis approach and a highly conductive support material makes N-CNF/EG a promising oxygen reduction catalyst for low temperature fuel cells.

1 Introduction

One of the major obstacles for the commercialization of fuel cells is the necessity for high cost noble metals to facilitate the electrode reactions. Especially the oxygen reduction reaction (ORR), the cathode reaction in fuel cells, is slow and requires high Pt loadings [1]. Design of cheaper materials to replace the noble metals without compromising with the activity has therefore received increasing scientific and industrial interest. Several types of non-noble catalysts have been explored over the years, with carbon nanomaterials containing nitrogen and trace amounts of transition metals being the most promising alternative [2,3]. Recently, it has even been reported that some of the N-doped carbon nanomaterials show higher ORR-activity, stability and crossover tolerance compared to conventional Pt-based catalysts in alkaline media [4–7]. However, in acidic conditions the ORR-activity and stability still remain lower than that of Pt [8–11].

Carbon nanofibers (CNFs) and carbon nanotubes (CNTs) are attractive as support materials in electrocatalytic applications due to their electrical conductivity, high degree of graphitization and corrosion resistance [12]. In addition, nitrogen-doping makes the CNFs and CNTs active for the ORR without the need for supported noble metal catalysts. One of the most versatile and economically competitive methods for producing N-CNFs and N-CNTs is chemical vapor deposition (CVD) [12,13]. In short the N-CNFs are grown by decomposing carbon and nitrogen precursors over transition metal catalysts such as iron, nickel and cobalt. Commonly used

variations of the CVD method for producing N-CNFs include aerosol assisted CVD, floating catalyst CVD and pyrolysis-type CVD [14]. The CVD technique offers the possibility for in situ N-doping of CNFs and CNTs by simply introducing a nitrogen precursor during the synthesis. A wide range of nitrogen sources have been employed including ammonia[15], pyridine[16], acetonitrile[17–19], melamine[20] and imidazole[21]. Ammonia might be the most convenient nitrogen precursor to employ because it is inexpensive, abundant, exists in gaseous form at room temperature and can easily be added to the precursor feed.

Some of the first to report the use of N-CNF electrodes for the reduction of oxygen was Maldonado and Stevenson [16]. Their catalyst was prepared by a floating CVD method using ferrocene and xylene, and showed significant activity towards the reduction of H_2O_2 in alkaline media. Ozkan's research group was among the first to demonstrate that N-CNFs also showed activity for the ORR in acidic media [22,23]. In their reports the catalysts were synthesized by decomposition of acetonitrile over silica, magnesia and Vulcan carbon supports impregnated with Fe-, Ni- or Co-acetate. In recent years several research groups have reported oxygen reduction activity for various forms of N-CNFs in both alkaline electrolyte [4,15,17] and acidic electrolyte [18,24]. However, complex growth precursors and synthesis procedures are often employed. Especially the use of oxide supports with low electronic conductivity makes purification steps such as refluxing in concentrated alkaline and acidic solution necessary before employing the N-CNFs in electrocatalytic applications. Harsh post treatment procedures not only complicates the synthesis, but also alters the surface chemistry and the catalytic properties of the N-CNFs [15,19,25].

Graphene and graphite are highly conductive materials that have been used as supports in a range of electrochemical energy technologies [26,27]. Unfortunately they are less suited as supports for N-CNF growth by the CVD method because graphite has low surface area and porosity, while graphene easily agglomerate or even restack upon drying [28]. Low cost natural flake graphite can however be intercalated with nitric or sulfuric acids, and a subsequent heat treatment leads to an expansion along the c-axis of the graphite increasing the volume and porosity. As opposed to graphene and graphite, expanded graphite (EG) exhibits a more stable porous structure and has been shown to be well suited for CNT growth [29,30].

In this report N-CNFs are prepared from Fe and Ni by in situ nitrogen-doping using ammonia as nitrogen precursor and carbon monoxide or ethane as carbon precursors in a catalytic CVD method. Furthermore, expanded graphite (EG) was used as support material for the N-CNF growth and due to its highly porous structure 20wt% metal nanoparticles could be loaded on the surface by incipient wetness impregnation. The electrocatalytic activity of the

as-grown N-CNF/EG was tested in both acidic and alkaline electrolytes and the N-CNFs prepared from Fe showed promising ORR-activity and stability. The combination of a single-step CVD process, simple gaseous precursors and graphite as support material makes this synthesis method promising for large scale production of N-doped carbon electrocatalysts.

2 Experimental

2.1 Synthesis

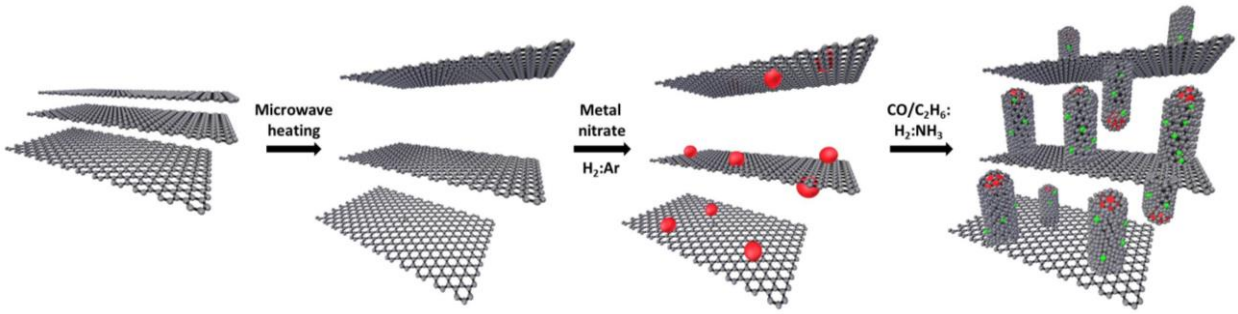

Figure 1 *Schematic illustration of the synthesis procedure showing metal nanoparticles (red balls) supported on expanded graphite, and carbon nanofibers doped with nitrogen (green balls).*

A schematic illustration of the synthesis procedure is shown in Fig. 1. First, expanded graphite was produced by heating oxidized graphite (Expandable Graphite GHL PX 95/350 N, Georg H. LUH GmbH, Germany) in a microwave oven at 700W for 60s. EG-supported iron or nickel catalysts with a metal loading of 20 wt% were prepared by incipient wetness impregnation of the support with metal nitrates (Iron(III)-nitrate nonahydrate, Fluka and Nickel(II)-nitrate hexahydrate, Fluka) dissolved in 96% ethanol. The growth catalysts were dried in room temperature for several days before being used.

Nitrogen-doped carbon nanofibers were synthesized using a catalytic CVD-method. The growth catalyst (0.2 g, 20wt% metal/EG) was loaded in a tubular quartz reactor and reduced in an H_2:Ar flow (40:160 ml/min, purity 5.0:5.0, AGA) by increasing the temperature of the furnace 3°C/min up to 650°C. Subsequently, N-CNFs were grown at 650°C using a synthesis gas mixture of C_2H_6:NH_3:H_2 (120:40:40 ml/min, purity 3.5:3.6:5.0, AGA) for Ni/EG, and CO:NH_3:H_2 (60:20:20 ml/min, purity 3.7:3.6:5.0, AGA) for Fe/EG. The obtained N-CNF/EG catalysts are denoted N-CNF/Ni and N-CNF/Fe respectively. The synthesis time was 4.5 hours for N-CNF/Ni and 24 hours for N-CNF/Fe. For comparison the synthesis on Fe/EG was also performed without CO in the reaction feed giving Fe/EG-NH_3, and without NH_3 in the reaction

feed giving CNF/Fe. The synthesis time was 24h for Fe/EG-NH_3 and 4h for CNF/Fe. After synthesis the reactor was cooled down to room temperature under an argon flow. A reference sample of reduced Fe nanoparticles on expanded graphite, Fe/EG-red, was prepared by cooling the reactor to room temperature under an Ar-flow after the reduction step.

2.2 Physicochemical characterization

The surface area of N-CNF/EG was characterized by N_2-adsorption measurements in a Micromeritics TriStar II 3020. Approximately 100 mg of the N-CNF/EG was degassed at 200 °C overnight prior to analysis. The specific surface area was calculated by the Brunauer-Emmet-Teller (BET) method.

The microstructure and morphology of N-CNF/EG was observed using a Hitachi S-5500 scanning transmission electron microscope (S(T)EM). The S(T)EM samples were prepared by attaching the N-CNF/EG to conductive carbon tape. Transmission electron microscopy (TEM) using a Jeol JEM-ARM200F equipped with a Jeol Centurio for X-Ray composition analysis by energy dispersive spectroscopy (EDS) was employed to characterize the N-CNF nanostructure. The TEM samples were prepared by dispersing N-CNF/EG in isopropanol by ultra-sonication. A drop of the dispersion was then deposited on a holey carbon film supported by a copper grid and dried at room temperature. The EDS data were acquired as spectrum images using the Gatan Digital Micrograph software.

Raman spectroscopy was employed to analyze the disorder in the N-CNF/EG using a Horiba Jobin Yvon LabRAM HR800 instrument. The samples were pressed between two glass slides and the spectra acquired with a laser excitation wavelength of 633 nm.

To identify the crystalline phases, X-ray diffraction (XRD) was performed using a Bruker D8 Advance DaVinci X-ray diffractometer with a LynxEye^{TM} detector and Cu Kα radiation (λ = 1.54 Å). The samples were prepared by using high vacuum grease to fix the carbon material to the sample holders. Measurements were done in the 2θ angular range 20º - 80º using a fixed slit of 0.6 mm. The diffractograms were analyzed using the software DIFFRAC.EVA and the PDF-4+ database from ICDD.

X-ray photoelectron spectroscopy (XPS) measurements were carried out in a Kratos Axis Ultra DLD spectrometer using monochromatic Al Kα radiation (hν = 1486.58 eV). Sample preparation was done by covering carbon tape with an even layer of catalyst powder. Survey spectra were collected using fixed analyzer pass energies of 160 eV while the high resolution spectra were collected at pass energies of 20 eV. Data analysis was performed using the

CasaXPS software. The elemental composition was calculated after the subtraction of Shirley-type backgrounds for the high resolution spectra. The N 1s region was deconvoluted using Gaussian-Lorentzian line shapes with 30% Lorentzian weighting.

Temperature-programmed oxidation (TPO) was performed in a Netzsch STA 449C thermo-microbalance coupled with a Netzsch QMS 403C *Aëolos*® mass spectrometer to analyze the oxidation products. Around 5-10mg of sample was loaded in the thermogravimetry (TG) instrument and heated from 40ºC to 900ºC at a rate of 10ºC/min under a flow of synthetic air (80mL/min, purity 5.0, AGA).

2.3 Electrochemical measurements

The electrochemical measurements were conducted in a conventional three-electrode setup using a reversible hydrogen electrode (RHE) as reference electrode and a platinum wire as counter electrode. All potentials reported in this paper are given versus the RHE. A rotating ring disk electrode (RRDE, disk: 5 mm ϕ, ring: Pt with 20 % collection efficiency) was used as working electrode. The N-CNF/EG catalysts were deposited on the glassy carbon disk electrode using the method described by Schmidt et al. [31]. A catalyst suspension was prepared by sonicating 1.0 mg of N-CNF/EG in a mixture of 600 µL Millipore H_2O, 300 µL 96% ethanol and 100 µL of 0.05 wt% Nafion® (DuPont™ DE521, Ion Power,Inc) for one hour. About 16 µL of the suspension was placed on the glassy carbon disk and dried under a N_2-flow. The procedure was repeated 2 times giving approximately 245 µg/cm^2 of N-CNF/EG catalyst deposited on the electrode surface. For comparison a commercial Pt/C catalyst (20wt% Pt on Vulcan XC-72R, E-TEK) was prepared by the same procedure giving a total of 245 µg/cm^2 of 20wt% Pt/C on the glassy carbon electrode.

Before performing the ORR the electrolyte was saturated with Ar and the electrodes were cleaned by performing cyclic voltammetry between 1.2 V and 0 V at different scanning rates. The background current was then measured by performing linear sweep voltammetry (LSV) from 1.10 V to 0.01 V at 5 mVs^{-1} in the Ar-saturated electrolyte. Oxygen reduction experiments were carried out in O_2-saturated 0.5M H_2SO_4 (95-97% H_2SO_4, Sigma Aldrich) and 0.5M KOH (extra pure KOH pellets, Merck) at room temperature. The potential range of the ORR was 1.10 V - 0.01 V, the scanning rate 5 mVs^{-1} and the rotational speed 1600 rpm. The third cathodic scan for N-CNF/EG and the third anodic scan for Pt/C after background subtraction are reported. Onset potentials for the oxygen reduction (E_{ORR}) were determined by comparing the LSV curve obtained in Ar with the ORR measurement. Finally, the stability test was performed

by cycling in the potential range 1.1 V - 0.6 V at 20 mVs^{-1} and 600rpm in O_2-saturated 0.5M H_2SO_4.

In order to detect the amount of H_2O_2 produced on the working electrode during the ORR, a constant potential of 1.2 V vs. RHE was applied to the Pt ring electrode. The H_2O_2 yield was calculated from the ring current (I_R), the disk current (I_D) and the collection efficiency of the Pt ring (N) using the following equation [32]:

$$H_2O_2\ (\%) = 200 \times \frac{(I_R / N)}{(I_R / N) + I_D} \qquad (1)$$

3 Results and discussion

3.1 Physicochemical characterization

S(T)EM images showing the surface morphology of the expanded graphite after N-CNF growth are presented in Fig. 2a-c. The graphite support was successfully expanded into a fluffy texture with low density as observed in Fig. 2a. Due to the abundant porous structure of the expanded graphite it was possible to achieve high loadings of metal nanoparticles on the graphite by simple incipient wetness impregnation. S(T)EM imaging of 20 wt% Fe/EG after reduction in H_2/Ar, Fig. 1d, show Fe nanoparticles with sizes ranging from a few nm up to 50nm distributed on the graphite surface. After the CVD process the surface of the expanded graphite was covered with N-CNFs of various diameters as displayed in Fig. 2b-c. The variation in N-CNF diameter could be related to the various sizes of the metal nanoparticles before growth. Furthermore, the N-CNF growth did not seem to change the structure of EG as seen in Fig.2a. On contrary, the growth of N-CNFs on the surface of EG might help preserve the fluffy EG structure by preventing it from collapsing. BET measurements showed that the surface area increased after N-CNF growth, from 35 m^2/g for expanded graphite to 226 m^2/g for N-CNF/Ni and 86 m^2/g for N-CNF/Fe. The difference in surface area for N-CNF/Ni and N-CNF/Fe was probably due to the difference in N-CNF yield since the N-CNF growth was faster on nickel compared to on iron.

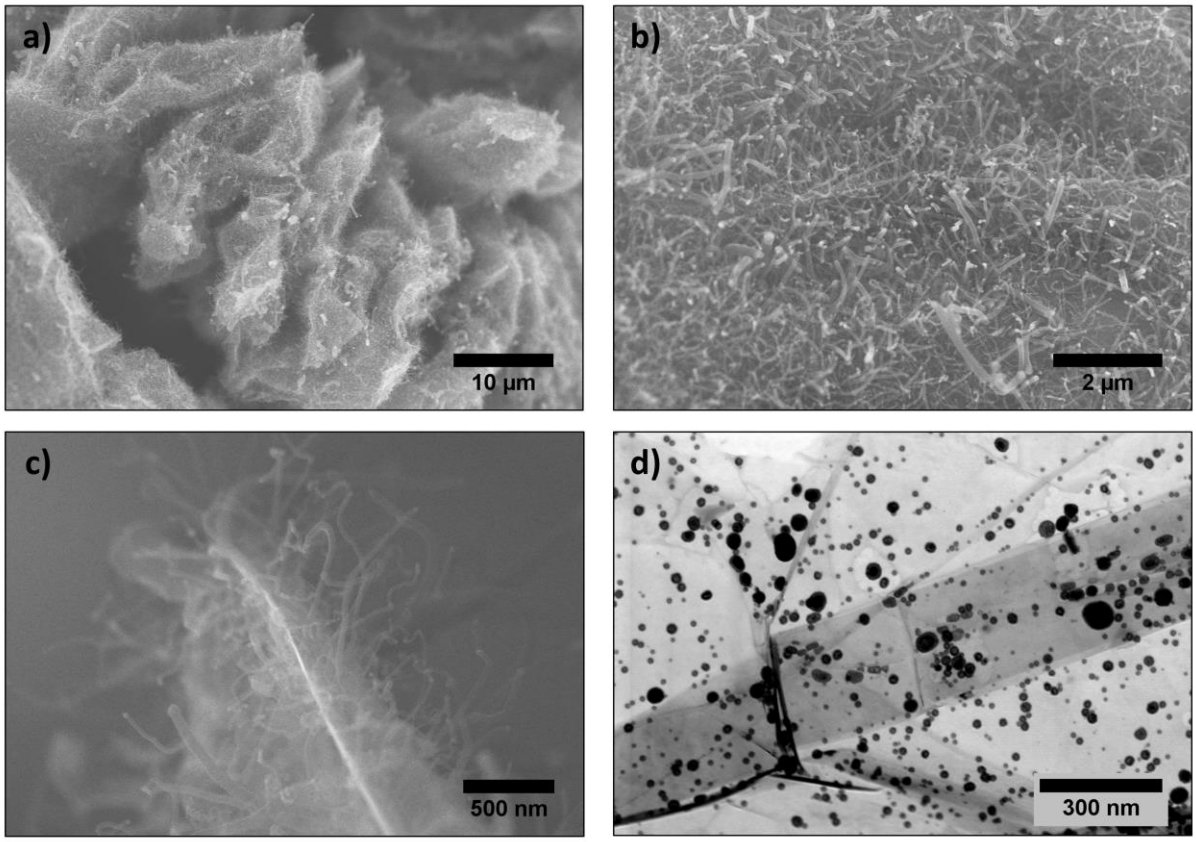

Figure 2: *S(T)EM images of N-CNF/Fe (**a-c**) and Fe nanoparticles on expanded graphite after reduction, Fe/EG-red (**d**).*

Higher magnification TEM images of the N-CNFs obtained from Fe and Ni supported on EG are presented in Fig. 3 and also show that the diameter of the N-CNFs varied in size. In addition the TEM images revealed the nanostructure of the N-doped carbon nanofibers. As shown in Fig. 3a-c, N-CNF/Fe consists of hollow nanofibers with a herringbone structure and a compartmentalized morphology inside the nanofibers. This bamboo like structure is typical for carbon nanotubes and carbon nanofibers containing nitrogen [33–35], but has also been identified for CNTs and CNFs grown from Fe on graphite [36,37]. Interestingly the N-CNF/Fe also showed smaller compartments in-between the graphene sheets in the surface of the N-CNFs. On the contrary, structural characterization of N-CNFs/Ni (Fig. 3 d-f) showed N-doped carbon nanofibers with more randomly oriented graphitic planes and no hollow core. It has been suggested by van Dommele et al. that the formation of a bamboo-structure for N-CNTs is related to the thermodynamic stabilities of the metal carbides [35]. Due to the higher solubility of carbon in Fe than in Ni, the probability for forming a graphitic envelope around Fe is higher than for Ni and can explain why a graphitic compartmentalization was only

observed for N-CNF/Fe. The carbon solubility might also explain why the Fe particles at the tip of the N-CNFs were encapsulated by a several nm thick layer of carbon (Fig. 3 b-c), while the Ni particles were fully exposed (Fig. 3f). Finally, the shape of the Fe and Ni nanoparticles could influence the morphology of the N-CNFs. As can be observed in Fig. 3b-c, the inner graphene layers of the N-CNFs grown on Fe follow the curvature of the sidewalls of the cone shaped Fe catalyst particles resulting in herringbone type nanofibers [38]. The Ni particles on the other hand exhibit a more spherical shape leading to N-CNFs with a more random structure.

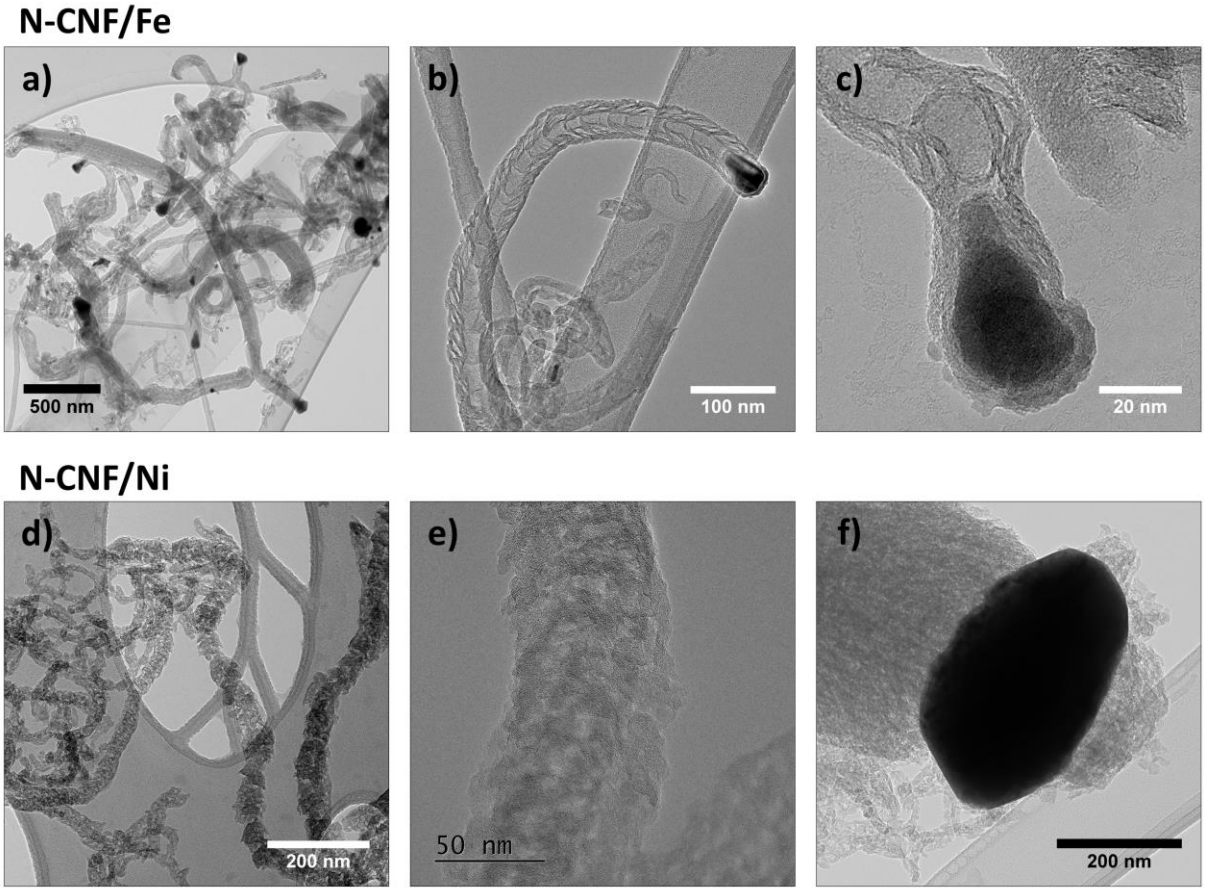

Figure 3 *TEM images of N-CNF/Fe (**a-c**) and N-CNF/Ni (**d-f**).*

Elemental mapping of the N-CNFs was done by EDS-analysis with the TEM working in STEM mode and the analysis of a single N-CNF from Fe and Ni is shown in Fig. 4a and 4b respectively. The elemental mapping of iron and nickel clearly shows that the metal particles are located at the tip of the N-CNFs and indicates that the nanofiber growth follows a tip-growth mechanism for both metals [13]. Furthermore, the examples shown are consistent with the tendency for Fe-particles to be cone shaped while the Ni-particles are more spherical. The

elemental mapping of oxygen shows that the surface of both the Fe- and Ni-particles is partly oxidized. The oxide layer for Ni is quite uniform since the Ni particles are exposed at the tip of the nanofiber (Fig. 4b). By comparison, the Fe particles have been partially protected from oxidation by being enclosed in the nanofibers and are only oxidized at the tip where they are covered by only a few layers of carbon (Fig. 4a). The EDS analysis also confirmed the presence of nitrogen in the N-CNFs and indicated that nitrogen was homogeneously distributed in both N-CNF/Fe and N-CNF/Ni. Even though the nitrogen signal was weak and susceptible to the influence of variations in the X-ray background level, the uniformity was confirmed by examination of spectra extracted from specific positions in the nanofibers.

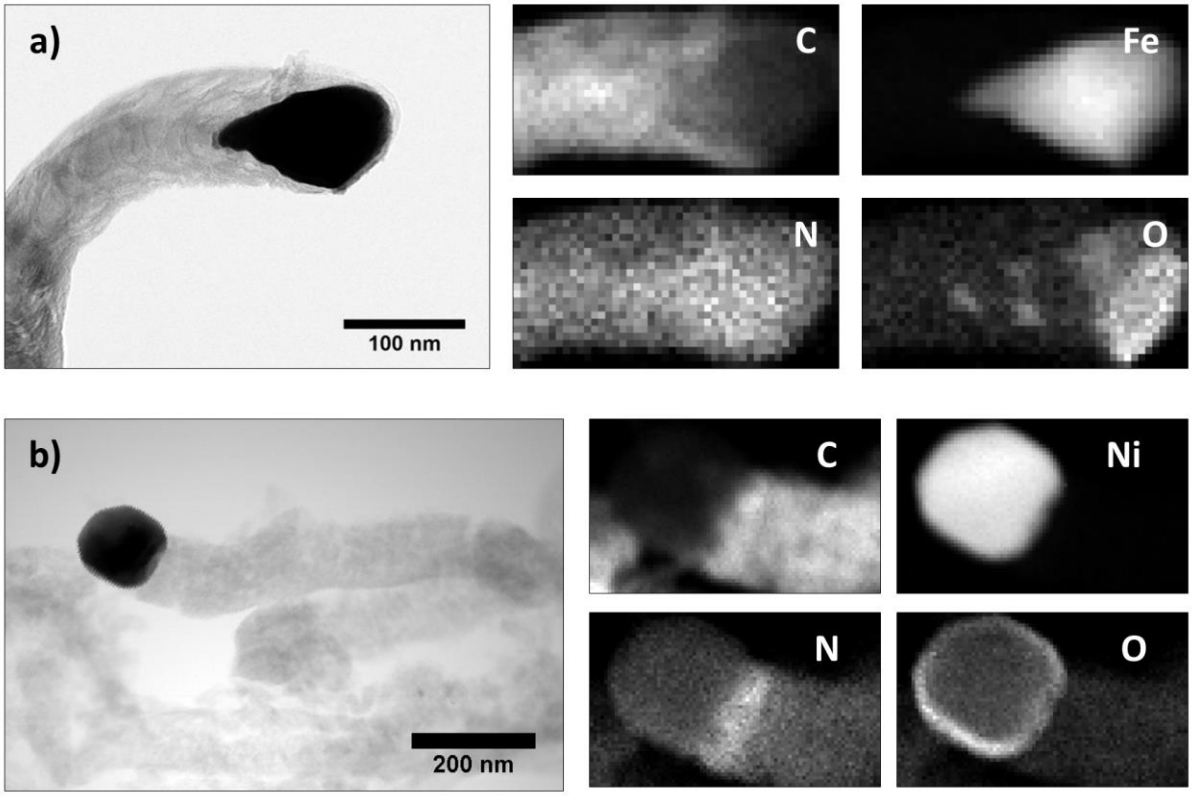

Figure 4 *Elemental maps from EDS-analysis with corresponding bright field STEM images for N-CNF/Fe (**a**) and N-CNF/Ni (**b**).*

Disorder in carbon materials can be assessed by Raman spectroscopy, and the Raman spectra of N-CNF/EG are compared with Fe/EG-red and Fe/EG-NH_3 in Fig. 5. The spectra for Fe/EG and Fe/EG-NH_3 show a prominent G-band at ~1577 cm^{-1} and a 2D-band at ~2683 cm^{-1}, both related to the sp^2 hybridization of graphite [39]. Disordered graphite such as edges of the graphene layers give rise to a D-band at ~1333 cm^{-1} and for Fe/EG-red an additional

shoulder in the G-band around 1618 cm^{-1} indicate the presence of a disorder induced D'-band. For N-CNF/Fe and N-CNF/Ni the N-doped carbon nanofibers also contribute to the Raman spectra resulting in an increase in the intensity of the D-band due to a higher degree of disorder in N-CNFs compared to graphite. It also seems that the 2D-band is only originating from the expanded graphite and is masked completely by the N-CNF signal for the Ni-sample. The ratio of the peak intensities I_D/I_G can be used to characterize the level of disorder in carbon materials, and indicates that N-CNF/Ni is more disordered than N-CNF/Fe. This corresponds well with the observed nanostructure of the N-CNFs where N-CNF/Ni shows more disordered fiber structure compared to N-CNF/Fe. The G-band in the Raman spectra is broadened for both N-CNF/EG samples, and for N-CNF/Ni the band is shifted to ~1590 cm^{-1} suggesting a strong contribution from the D'-band. These characteristics are similar to the Raman spectra reported by Choi et al. for N-doped graphene/carbon nanotube composites [40] and Tang et al. for N-doped carbon nanotube cups [17].

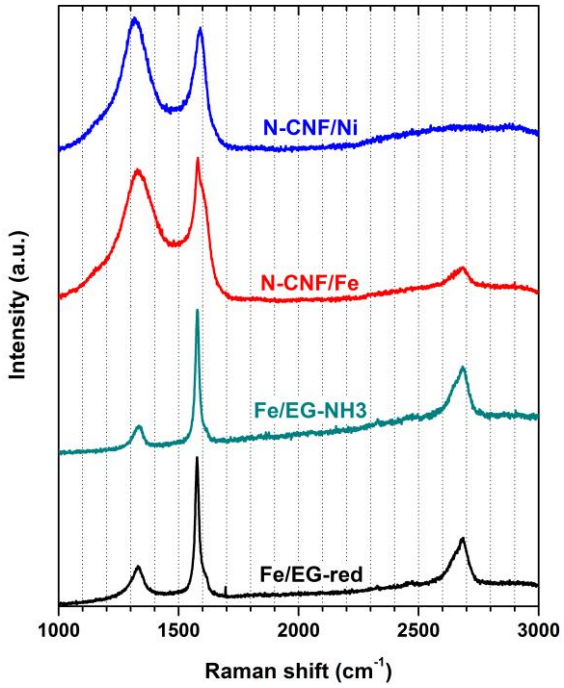

Figure 5 *Raman spectra of Fe/EG-red, Fe/EG-NH_3, N-CNF/Fe and N-CNF/Ni obtained with an excitation wavelength of 633 nm.*

X-ray diffractograms of N-CNF/Fe and N-CNF/Ni are presented in Fig. 6 together with Fe/EG-red, Fe/EG-NH_3 and CNF/Fe for reference. All samples showed a strong reflection at $2\theta = 26.5^{o}$ corresponding to the (002) peak of graphite (PDF 00-056-0159), see Fig. 6a. For N-CNF/Ni the peak was broad indicating that the carbon was less crystalline. Moreover, all the

Fe-based samples showed additional graphite reflections at 54.7º (004) and 77.5º (110), which were not detectable in N-CNF/Ni. By using reference files from the ICDD database, the strongest remaining reflections in Fe/EG-red, Fe/EG-NH_3 and CNF/Fe were identified as α-Fe (PDF 04-007-9753), Fe_4N (PDF 04-012-3036) and Fe_5C_2 (PDF 04-014-4562) respectively (Fig. 6b). For N-CNF/Fe the XRD pattern seemed to consist of contributions from iron, iron nitride and iron carbide. However, no iron oxide could be identified. The XRD peaks for N-CNF/Ni were identified as metallic nickel (PDF 00-001-1258), Ni_3C (PDF 00-006-0697), as well as NiO (PDF 04-011-2340). The presence of a metal oxide for N-CNF/Ni and not for N-CNF/Fe was probably due to the encapsulation of the Fe-particles by carbon resulting in only a minor oxidation as observed by TEM and EDS characterization (Fig. 3 and Fig. 4).

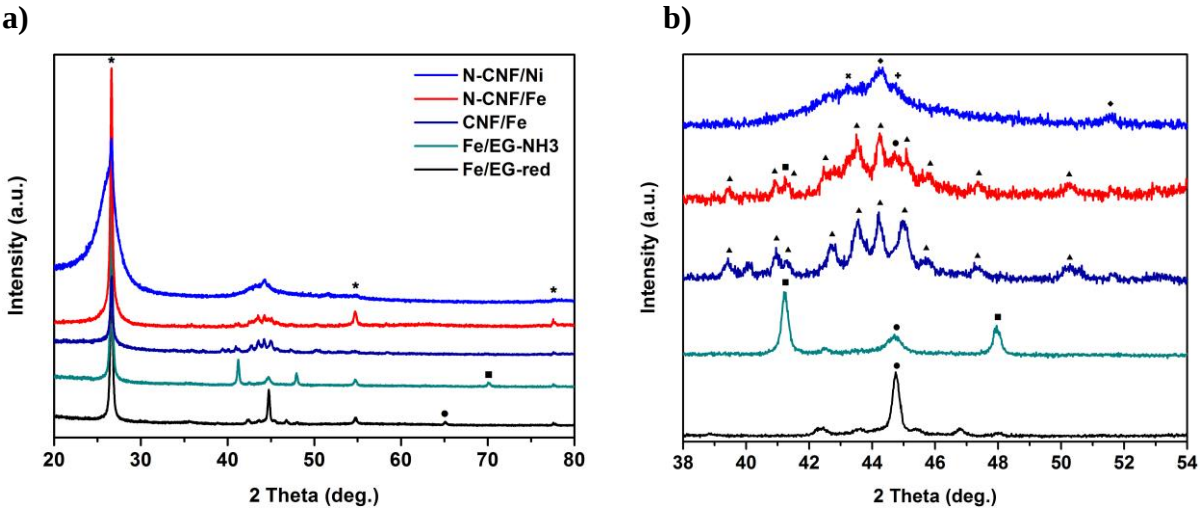

Figure 6 *Full XRD pattern (**a**) and magnification of the main metal peaks (**b**). The peaks were identified as graphite (*), iron (●), iron nitride (■), iron carbide (▲), nickel (♦), nickel carbide (**+**) and nickel oxide (**x**).*

X-ray photoelectron spectroscopy was employed to study the elemental composition and nitrogen distribution in the surface of the N-CNFs, Fig. 7. The elemental composition of N-CNF/Fe and N-CNF/Ni calculated from high resolution measurements of each element is shown in Table 1. The metal content detected in XPS is much lower than the initial metal loading of 20wt% metal on EG. This is mainly due to N-CNF growth, carbon encapsulation and the formation of oxide layers in the surface of the metal particles. A lower metal content was observed for N-CNF/Ni which is due to the higher growth yield during the N-CNF synthesis resulting in a lower metal/carbon ratio compared to N-CNF/Fe. Furthermore, the N-

CNF/Ni contained considerably less nitrogen and oxygen than the N-CNF/Fe. A possible explanation can be that the carbon nanofiber formation rate is much faster than the rate of decomposition of NH_3 on the nickel particles. Consequently, the percentage of nitrogen atoms incorporated in the carbon structure was lower than for N-CNF/Fe. The competitive reaction kinetics between the decomposition of carbon precursor and nitrogen precursor could influence both the nitrogen content and the nature of the nitrogen incorporation.

The binding configurations of the nitrogen atoms in the N-CNFs were analyzed by high resolution XPS for the N 1s region as shown in Fig. 7b-c. Deconvolution of the XPS spectra showed the presence of 5 peaks for both N-CNF/Fe and N-CNF/Ni which are similar to the peaks reported by Kundu et al [18]. The contributions of the different nitrogen species to the N 1s peak are summarized in Table 1. The two main peaks present, N1 and N3, were located at 398.4eV and 401.0eV and were identified as pyridinic nitrogen and quaternary nitrogen respectively [41,42]. As much as 48% of the nitrogen was incorporated as pyridinic nitrogen in N-CNF/Fe (Fig. 7b) and 32% as quaternary nitrogen. For N-CNF/Ni (Fig. 7c), quaternary nitrogen was the most abundant N-species with 41%, followed by pyridinic nitrogen which contributed to 27% of the nitrogen detected. In addition three smaller peaks were observed from the deconvolution of the N 1s spectrum at 399.5eV (N2), 402.1-402.6eV (N4) and 403.7-404.5eV (N5). The region above 402eV in N1s XPS spectra is generally attributed to nitrogen-oxygen bonds [43]. The N4 peak was therefore assigned as pyridinic oxide and the N5 peak to other forms of oxidized nitrogen species [42,44]. It was not possible to assign the N2 peak to any particular N-group since there are several nitrogen species with binding energy around 399.5eV; amino groups attached to aromatic rings, amide groups and transition metals coordinated to nitrogen [41,45]. XPS measurements were also performed for Fe/EG-NH_3 and CNF/Fe and the survey spectra are shown in Fig. 7a. There was no nitrogen detected for Fe/EG-NH_3 which implies that all the nitrogen observed in N-CNF/Fe and N-CNF/Ni originate from N-doping of the carbon nanofibers and not of the expanded graphite.

a)

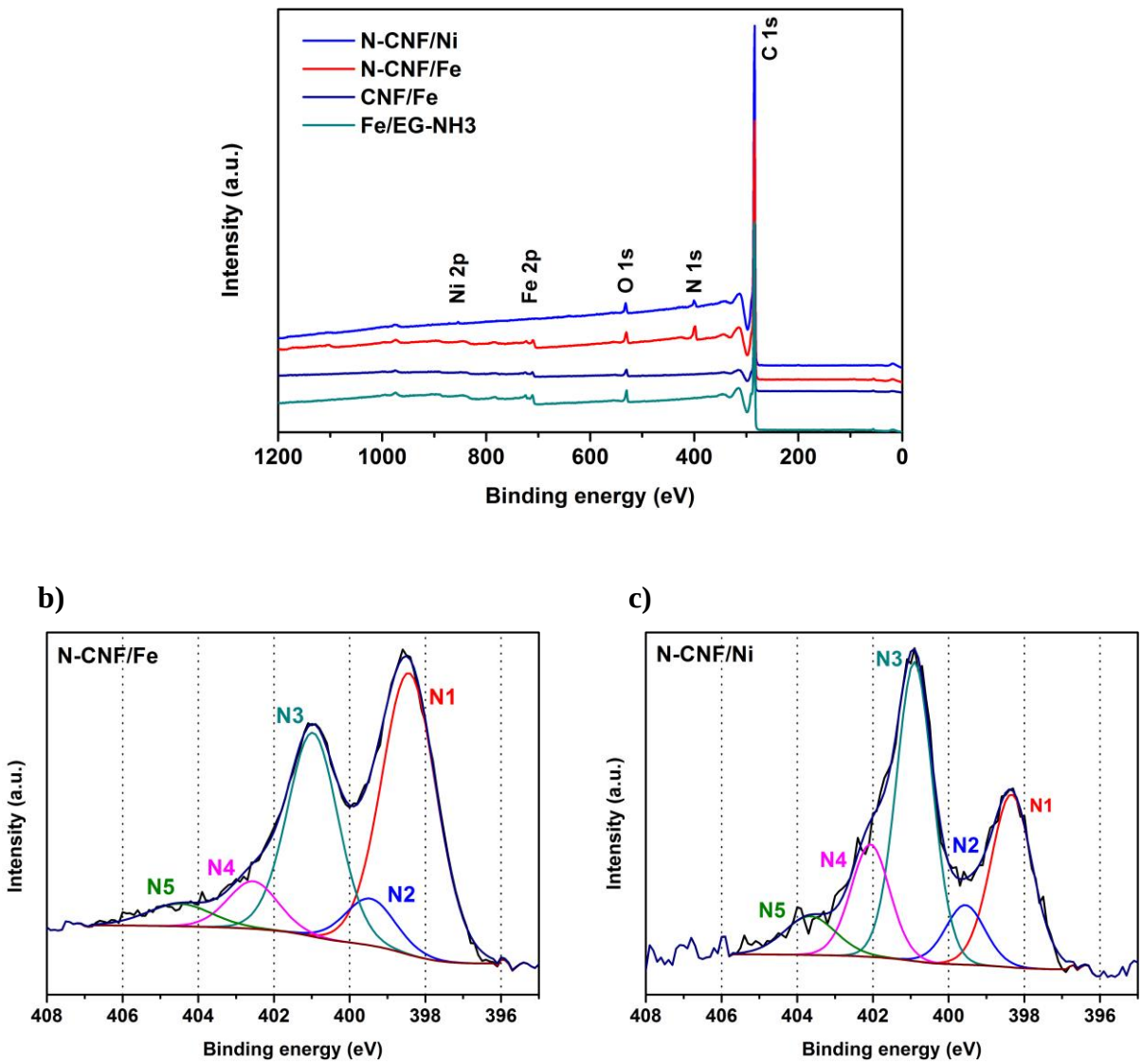

Figure 7 *XPS survey spectra (**a**) and high resolution spectra of the N 1s region for N-CNF/Fe (**b**) and N-CNF/Ni (**c**).*

Table 1 *Elemental composition and nitrogen groups present in N-CNF/Fe and N-CNF/Ni obtained from XPS analysis.*

	N *(at%)*	**O** *(at%)*	**Fe** *(at%)*	**Ni** *(at%)*	**N1** *(%)*	**N2** *(%)*	**N3** *(%)*	**N4** *(%)*	**N5** *(%)*
N-CNF/Fe	3.9	1.7	0.35	-	48.3	7.3	32.4	7.4	4.5
N-CNF/Ni	1.5	0.8	-	0.05	26.8	8.8	40.7	16.3	7.4

Temperature programmed oxidation was used to investigate the thermal stability of the N-CNF/EG and is shown in Fig. 8a. The CNF and N-CNF samples showed two separate oxidation regions, one at temperatures between 400-600ºC and another above 650 ºC. By correlating these measurements with the TPO profile of Fe/EG-red the oxidation taking place above 650ºC was attributed to expanded graphite. Thus, the oxidation taking place at lower temperatures was due to CNF or N-CNF oxidation. The bulk oxidation temperature for the N-CNFs grown on Fe was 430ºC and considerably lower than for CNF/Fe (600ºC) and N-CNF/Ni (590ºC). Since nitrogen doping induces defects in the carbon structure a lower thermal stability is expected for N-doped CNFs compared to undoped CNFs. In addition, XPS analysis showed that the N-content for N-CNF/Ni was lower than for N-CNF/Fe which may explain the higher oxidation resistance for the Ni sample.

The products formed during the oxidation of N-CNF/EG was monitored by coupling the TG-instrument to a mass spectrometer and the signal for CO_2 (m/z=44) and NO (m/z=30) are displayed in Fig. 8b-c. The CO_2 signal corresponds well with the two oxidation peaks related to N-CNF and EG for both N-CNF/Ni and N-CNF/Fe. However, the NO signal was only observed in the temperature range corresponding to N-CNF oxidation. This indicates that the nitrogen is only incorporated in the N-CNFs and not in the EG as was already suggested from the XPS analysis on Fe/EG-NH_3. The signal from NO_2 (m/z=46) (not shown) was also measured, but appeared to be a contribution from the CO_2 signal since it had a lower intensity than the NO signal and showed the exact same shape as the CO_2 signal [46].

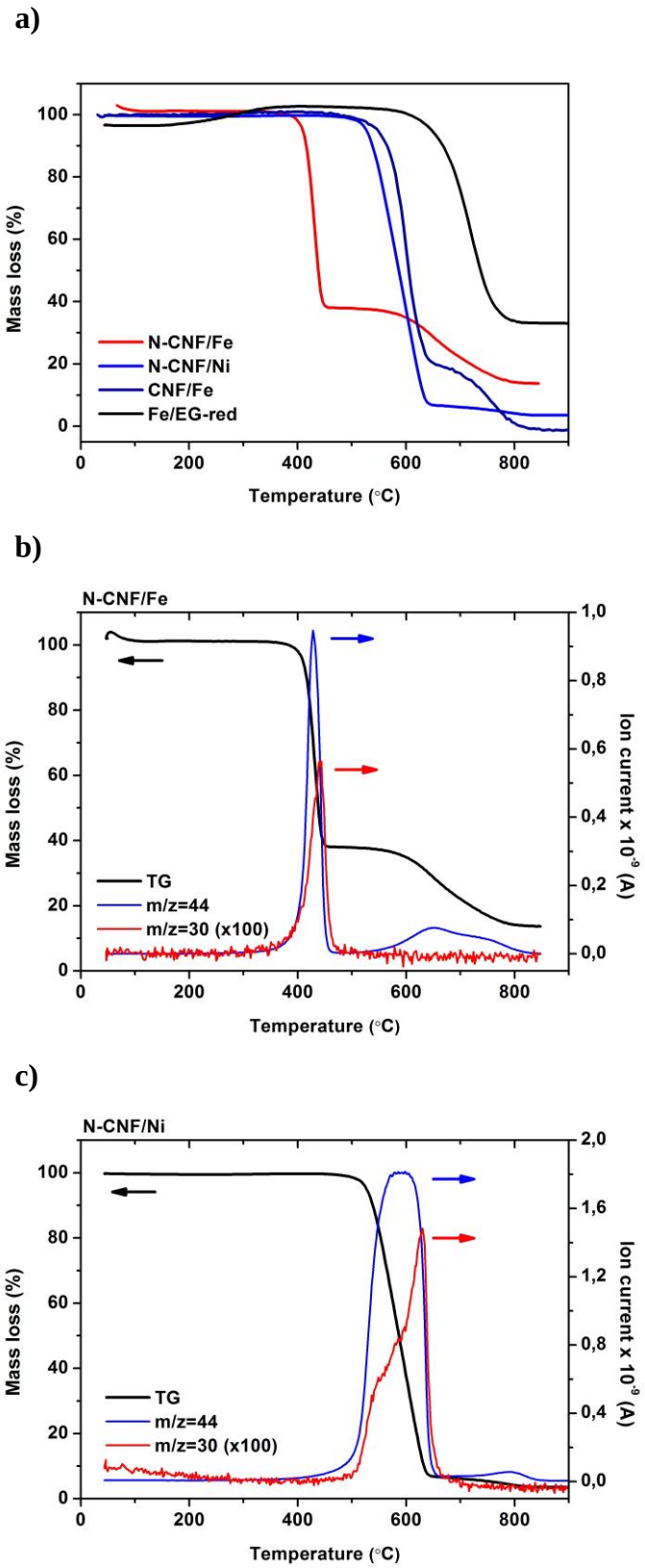

Figure 8 *Temperature programmed oxidation conducted in synthetic air at a heating rate of 10°C (**a**). TG-profile combined with CO_2 (m/z=44) and NO (m/z=30) signal for N-CNF/Fe (**b**) and N-CNF/Ni (**c**).*

3.2 Electrocatalytic activity for the ORR

The performance of the N-CNF/EG as electrocatalysts for the ORR in 0.5M H_2SO_4 is shown in Fig. 9a. Corresponding onset potentials for the oxygen reduction are given in Table 2 and were 0.93V for N-CNF/Fe and 0.65V for N-CNF/Ni. For reference a traditional Pt/C catalyst with high precious metal loading (245 μg/cm^2 20wt% Pt/E-TEK) is included and shows an oxygen reduction onset potential of 1.05V. Furthermore, the amount of hydrogen peroxide formed during the ORR was measured using a RRDE with a Pt-ring and calculated using eq. (1), see Fig. 9b. The oxygen reduction on N-CNF/Ni was highly selective towards H_2O_2 and as much as 85% of the oxygen was reduced to hydrogen peroxide following a two electron pathway. For N-CNF/Fe the H_2O_2 formation was significantly lower and ranged from 20-30% depending on the applied overpotential, with a maximum in H_2O_2 yield at 0.55V. N-CNF/Fe therefore seems to be more selective towards the four electron pathway for the ORR reducing most of the oxygen to water. The relatively high amounts of hydrogen peroxide detected for the N-CNF/EG catalysts could be related to the low catalyst loadings used on the electrode (245 μg/cm^2). Previous studies have shown that the probability for further reduction of hydrogen peroxide to water within the catalyst layer increases with catalyst loading on the electrode [47,48].

In order to exclude contributions from expanded graphite, iron particles and carbon on the ORR-activity of N-CNF/Fe, oxygen reduction was also performed using Fe/EG-red, Fe/EG-NH_3 and CNF/Fe as catalysts (Fig. 9c-d). The Fe/EG-NH_3 obtained by performing the CVD without CO in the feed displayed an increase in ORR-activity compared to Fe/EG-red. Furthermore, both Fe/EG-NH_3 and CNF/Fe showed ORR onset potentials of 0.82V, but only notable ORR currents at very high overpotentials. Although no nitrogen could be detected in Fe/EG-NH_3 by XPS, XRD analysis confirmed the presence of iron nitride in the bulk which could be the reason for the improved ORR-activity compared to Fe/EG-red. On the other hand, CNF/Fe was prepared without any nitrogen precursor in the feed and thus contained no nitrogen or iron nitride as confirmed by XPS and XRD analysis. However, the presence of iron carbide was revealed by XRD and might be the origin of the observed ORR-activity. For CNF/Fe a sudden increase in ORR current was observed at 0.3V and seemed to be related to the two electron reduction of oxygen to hydrogen peroxide since the H_2O_2 yield detected on the ring increased simultaneously (Fig. 9d). In conclusion, the ORR activity observed for N-CNF/Fe does not seem to originate from expanded graphite, iron, iron nitride, iron carbide or carbon since their ORR currents were negligible in comparison.

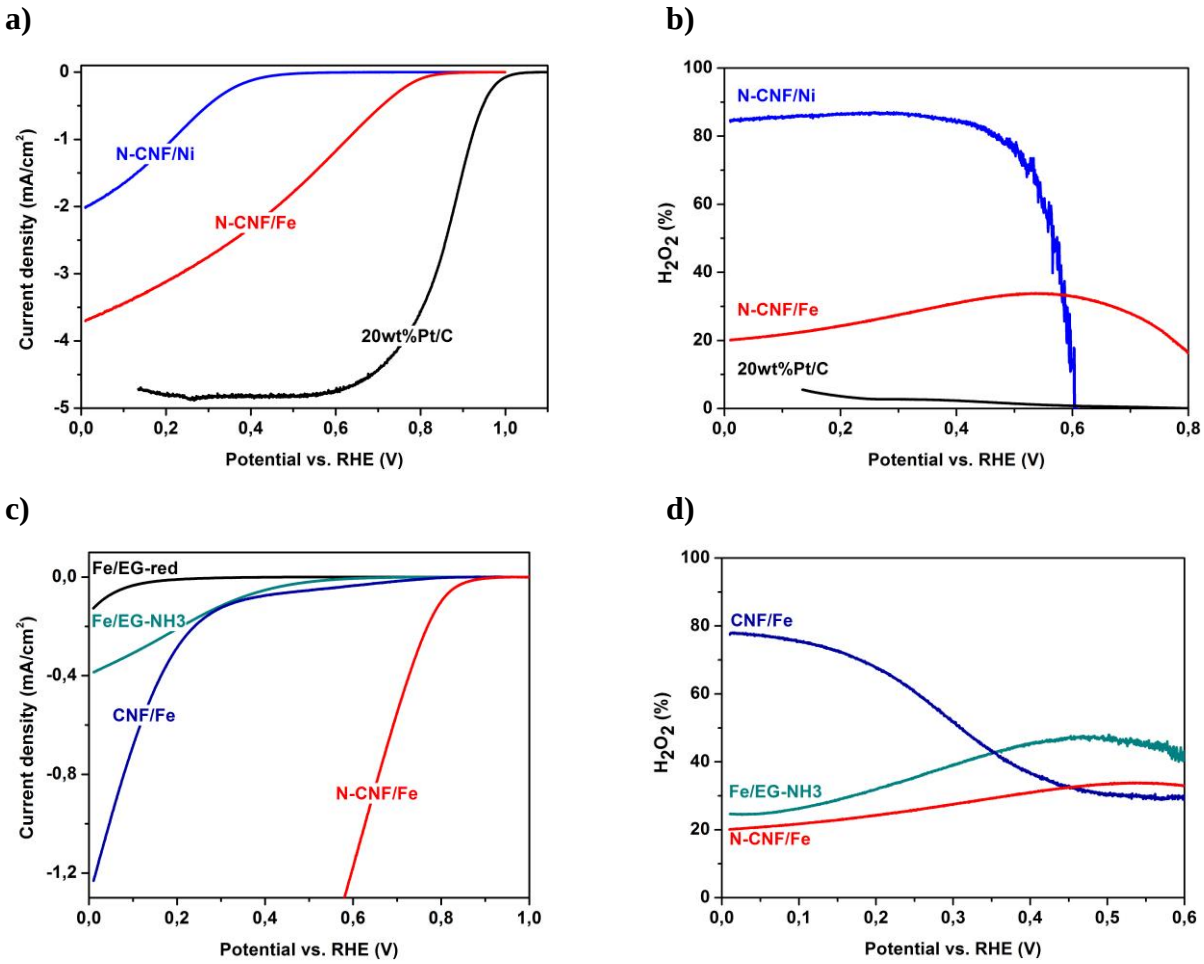

Figure 9 *Polarization curves at 5 mVs^{-1} and 1600 rpm for the oxygen reduction in 0.5M H_2SO_4 (**a** and **c**). The amount of hydrogen peroxide formed during the ORR calculated from the Pt-ring current (**b** and **d**). The catalyst loading was 245 µg cm^{-2}.*

Table 2 *Oxygen reduction onset potentials vs. RHE in 0.5M H_2SO_4 and 0.5M KOH.*

Sample	E_{ORR} (acid)	E_{ORR} (alkaline)
Fe/EG-NH_3	0.82 V	-
CNF/Fe	0.82 V	-
N-CNF/Ni	0.65 V	0.95 V
N-CNF/Fe	0.93 V	1.07 V
20wt% Pt/C	1.05 V	1.09 V

In alkaline electrolyte the N-CNFs on expanded graphite showed higher activity for the ORR compared to in acidic electrolyte as shown in Fig. 10a. The onset potentials for the ORR in 0.5M KOH increased to 0.95V for N-CNF/Ni and 1.07 V for N-CNF/Fe which is close to

the onset potential for the commercial Pt/C catalyst (1.09V). The increase in ORR-activity with pH has been reported for many different nitrogen-doped carbon nanomaterials [21,48,49], and has been attributed to the weaker adsorption of anions on the surface of the catalyst in alkaline electrolytes [50]. Furthermore, the yield of the intermediate product HO_2^- from the two electron reduction process in alkaline electrolyte decreased considerably at low overpotentials for N-CNF/Fe. Only 1% HO_2^- was detected on the Pt-ring at 0.8V in 0.5M KOH as displayed in Fig. 10b. The HO_2^- yield changed with applied overpotential and went through a maximum at 0.55V as was also observed in 0.5M H_2SO_4. For N-CNF/Ni the amount of HO_2^- produced in 0.5M KOH was 70%, which is 10% lower than the amount of H_2O_2 produced in acidic electrolyte. The decrease in HO_2^- formation for N-CNFs in alkaline electrolyte could be related to the improved residency time of the peroxide intermediates at the catalyst surface facilitating the 4-electron reduction of oxygen [51,52].

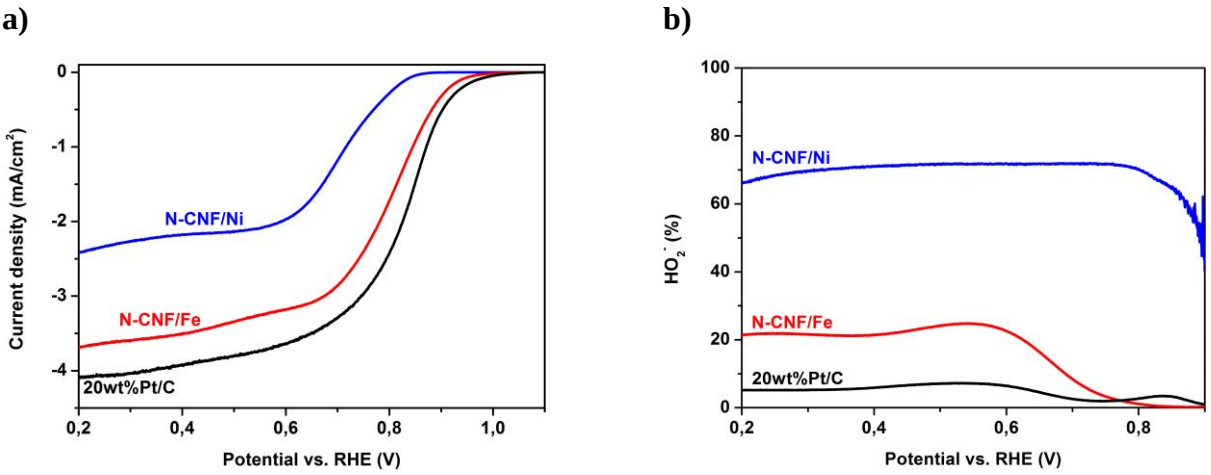

Figure 10 *Polarization curves at 5 mVs^{-1} and 1600 rpm for the ORR in 0.5M KOH (**a**), and hydrogen peroxide detected on the Pt-ring (**b**). The catalyst loading was 245 $\mu g\ cm^{-2}$.*

In addition to showing a promising onset potential for the ORR, the oxygen reduction current for N-CNF/Fe was also notable considering the low catalyst loading used on the electrode (245 $\mu g/cm^2$), and the high Pt loading used as reference (49 $\mu g_{Pt}/cm^2$). By accounting for the loading of N-CNF/Fe on the electrode an ORR-current of 4.9 mA/mg is obtained at 0.6V in acidic electrolyte, and 7.0 mA/mg at 0.8V in alkaline electrolyte. Thus, the ORR activity of N-CNF/Fe is higher than recently reported for N-CNFs and N-CNTs in terms of both onset potential and current [15,18,19,21]. Moreover, the RRDE measurements showed that the N-CNFs grown from Fe were much better oxygen reduction catalysts than the N-CNFs grown from Ni. This is in agreement with the results from Matter et al. [23] and Tang et al.

[17] who have shown that N-CNTs/N-CNFs prepared from Fe have higher ORR-activity than catalysts prepared from Ni.

Even though the active sites for the oxygen reduction on N-doped carbons have yet to be identified, most studies suggest that the presence of iron during the synthesis procedure is beneficial for achieving an active catalyst [53]. Iron being part of the active site has therefore been suggested as an explanation for why N-doped carbon nanostructures prepared by Ni show lower ORR activity compared to the ones prepared from Fe. In our study the presence of iron in N-CNF/Fe is evident and has been confirmed by TEM, EDS, XRD, TPO and XPS analysis. However, by testing reference samples of Fe/EG-red, Fe/EG-NH_3 and CNF/Fe for the ORR the contribution from metallic iron, iron carbide, iron nitride and CNFs grown from Fe could be ruled out. Thus, if iron is part of the active site it must be incorporated in the N-CNFs as a metal-nitrogen-carbon compound. DFT calculations have suggested that such Fe-N_x moieties can be identified in XPS N1s spectra at binding energies ~1eV higher than the position of N in a pyridinic environment [45]. In Fig. 7b, the deconvolution of the N1s spectra for N-CNF/Fe showed a peak at 399.5eV, which is 1.1eV higher than the pyridinc-N peak (398.4eV). However, this peak position can also be attributed to amine (399.3eV), and since the N-CNFs are produced by decomposition of NH_3 it is more appropriate to attribute the peak to the presence of NH_2-groups rather than Fe-N_x. Further analysis is therefore needed to reveal whether Fe-N_x moieties are present in N-CNFs grown from Fe.

For N-CNFs prepared by catalytic CVD the transition metal can also contribute to the ORR activity indirectly by influencing the chemical properties of the N-CNFs. TEM imaging (Fig. 3) revealed that N-CNF/Fe exhibited a characteristic bamboo-like structure while N-CNF/Ni had a more random structure. However, it is not likely that the bamboo-structure contributes notably to the catalytic activity as this microstructure has been obtained for several different transition metals without resulting in the same ORR-activity [17]. Moreover, the choice of transition metal can affect the decomposition rate of the carbon and nitrogen precursors which in turn will influence the incorporation of nitrogen in the N-CNFs. XPS characterization (Fig. 7) showed that N-CNF/Fe contained more nitrogen than N-CNF/Ni, with pyridinic-N and quaternary-N being the primary nitrogen components. Ozkan and co-workers have suggested that there is a correlation between the amount of pyridinic nitrogen, exposed edge planes and the ORR activity of N-CNFs, and used this to explain the higher ORR activity for N-CNFs from Fe compared to N-CNFs from Ni [24,54]. Furthermore, Mo et al. found a correlation between the amount of pyridinic nitrogen present in N-CNTs and the ORR-activity [21]. In contrast, Popov's research group considered both pyridinic and quaternary nitrogen groups

important for creating active sites for the ORR in their N-doped carbon materials [55,56]. DFT calculations have also shown that both graphitic and pyridinic nitrogen can be involved in the oxygen reduction on N-doped carbon [57,58]. Thus, the high ORR-activity of N-CNF/Fe compared to N-CNF/Ni could simply be explained by the high amounts of both pyridinic and quaternary nitrogen groups in N-CNF/Fe.

The durability of the most active catalyst, N-CNF/Fe, was tested by performing potential cycling between 0.6V and 1.1V at a scan rate of 20 mVs^{-1} in O_2-saturated 0.5M H_2SO_4. The ORR polarization plots and the H_2O_2 formation before and after cycling are shown in Fig. 11. After 1600 cycles no significant changes were observed in the electrocatalytic activity and selectivity of the N-CNF/Fe. The catalyst showed a well-preserved onset potential for the oxygen reduction reaction of 0.92V after 1600 cycles, as well as a stable diffusion limited ORR-current. The high stability of the N-CNF/Fe catalyst may be due to the high content of graphitic carbon in N-doped CNFs which is more resistant towards oxidation compared to amorphous carbon [59]. In addition, the iron nanoparticles in N-CNF/Fe were encapsulated by several layers of graphite which might prevent the dissolution of Fe. Nevertheless, a small shift of the reduction current in the mixed kinetic-diffusion region of about 40 mV and an increase in the H_2O_2 formation of 2-3% was observed after the stability test. This indicates a slight change in the ORR kinetics for the N-CNF/Fe catalyst over time. Popov and co-workers suggested that the performance degradation of their nitrogen-modified carbon-based catalysts in acidic electrolyte was due to the protonation of pyridinic nitrogen groups [49,60]. However, they also reported a decrease in the limiting current which was not observed for the N-CNF/Fe catalyst. Herranz et al. further ascribed a decrease in ORR-activity of Fe/N/C catalysts in acidic medium to anions bonded to protonated nitrogen groups [61], which could also be the case for the N-CNFs grown from Fe.

a) **b)**

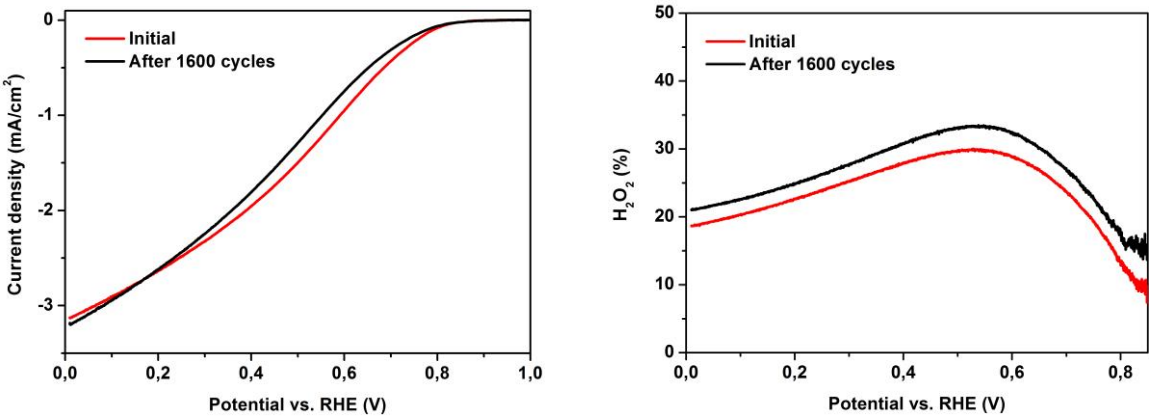

Figure 11 *Stability test of N-CNF/Fe in O_2-saturated 0.5M H_2SO_4 showing the LSV for the oxygen reduction at 5 mVs^{-1} and 1600 rpm (**a**), and the H_2O_2 detected on the Pt-ring during the ORR (**b**). The catalyst loading was 245 µg cm^{-2}.*

4 Conclusion

Nitrogen-doped carbon nanofibers supported on expanded graphite were successfully synthesized from Fe and Ni nanoparticles by a single-step CVD method using simple gaseous precursors. Characterization of the N-CNFs revealed differences in the microstructure, nitrogen content and nitrogen composition depending on the growth catalyst used during synthesis. Due to the high electronic conductivity of the expanded graphite support the N-CNF/EG were used directly as catalysts for the oxygen reduction reaction (ORR) without the need for harsh post-treatment procedures. The N-CNFs grown from Fe demonstrated high ORR onset potentials and selectivity towards the 4-electron pathway in both acidic and alkaline electrolyte. Furthermore, the N-CNF/Fe showed excellent durability after 1600 cycles in O_2-saturated 0.5M H_2SO_4. The versatile and easily scalable synthesis approach makes the N-CNF/EG a promising electrocatalyst for the ORR in low temperature fuel cells.

Acknowledgements

Financial support for this work was provided by the Norwegian University of Science and Technology (NTNU) and by the European Commision 7th Framework Programme (FP7) through the FREECATS project (grant no. 280658). The TEM work was carried out at the NORTEM Gemini Centre at NTNU and supported by the NORTEM project (grant no. 197405) within the INFRASTRUCTURE program of the Research Council of Norway (RCN).

NORTEM was co-funded by the RCN and the project partners NTNU, University of Oslo and SINTEF. Ida Hjorth (NTNU) and Anne Helene Barsnes (NTNU) are gratefully acknowledged for the S(T)EM analysis.

References

[1] Gasteiger HA, Kocha SS, Sompalli B, Wagner FT. Activity benchmarks and requirements for Pt, Pt-alloy, and non-Pt oxygen reduction catalysts for PEMFCs. Appl Catal B Environ 2005;56:9–35. doi:10.1016/j.apcatb.2004.06.021.

[2] Bezerra CWB, Zhang L, Lee K, Liu H, Marques ALB, Marques EP, et al. A review of Fe–N/C and Co–N/C catalysts for the oxygen reduction reaction. Electrochim Acta 2008;53:4937–51. doi:10.1016/j.electacta.2008.02.012.

[3] Chen Z, Higgins D, Yu A, Zhang L, Zhang J. A review on non-precious metal electrocatalysts for PEM fuel cells. Energy Environ Sci 2011;4:3167. doi:10.1039/c0ee00558d.

[4] Gong K, Du F, Xia Z, Durstock M, Dai L. Nitrogen-doped carbon nanotube arrays with high electrocatalytic activity for oxygen reduction. Science 2009;323:760–4. doi:10.1126/science.1168049.

[5] Qu L, Liu Y, Baek J-B, Dai L. Nitrogen-doped graphene as efficient metal-free electrocatalyst for oxygen reduction in fuel cells. ACS Nano 2010;4:1321–6. doi:10.1021/nn901850u.

[6] Geng D, Chen Y, Chen Y, Li Y, Li R, Sun X, et al. High oxygen-reduction activity and durability of nitrogen-doped graphene. Energy Environ Sci 2011;4:760. doi:10.1039/c0ee00326c.

[7] Chung HT, Won JH, Zelenay P. Active and stable carbon nanotube/nanoparticle composite electrocatalyst for oxygen reduction. Nat Commun 2013;4:1922. doi:10.1038/ncomms2944.

[8] Wu G, More KL, Johnston CM, Zelenay P. High-performance electrocatalysts for oxygen reduction derived from polyaniline, iron, and cobalt. Science 2011;332:443–7. doi:10.1126/science.1200832.

[9] Li Y, Zhou W, Wang H, Xie L, Liang Y, Wei F, et al. An oxygen reduction electrocatalyst based on carbon nanotube-graphene complexes. Nat Nanotechnol 2012;7:394–400. doi:10.1038/nnano.2012.72.

[10] Peng H, Mo Z, Liao S, Liang H, Yang L, Luo F, et al. High Performance Fe- and N- Doped Carbon Catalyst with Graphene Structure for Oxygen Reduction. Sci Rep 2013;3. doi:10.1038/srep01765.

[11] Kang S, Shen PK. A resin-based methodology to synthesize N-doped graphene-like metal-free catalyst for oxygen reduction. Electrochim Acta 2014;142:182–6. doi:10.1016/j.electacta.2014.07.100.

[12] Dai L, Xue Y, Qu L, Choi H-J, Baek J-B. Metal-Free Catalysts for Oxygen Reduction Reaction. Chem Rev 2015. doi:10.1021/cr5003563.

[13] Koziol K, Baskovic BO, Yahya N. Synthesis of Carbon Nanostructures by CVD method. In: Yahya N, editor. Carbon and Oxide Nanostructures, Berlin, Heidelberg: Springer; 2011, p. 23–49.

[14] Shao Y, Sui J, Yin G, Gao Y. Nitrogen-doped carbon nanostructures and their composites as catalytic materials for proton exchange membrane fuel cell. Appl Catal B Environ 2008;79:89–99. doi:10.1016/j.apcatb.2007.09.047.

[15] Truong-Phuoc L, Duong-Viet C, Doh W-H, Bonnefont A, Janowska I, Begin D, et al. Influence of the reaction temperature on the oxygen reduction reaction on nitrogen-doped carbon nanotube catalysts. Catal Today 2015;249:236–43. doi:10.1016/j.cattod.2014.11.020.

[16] Maldonado S, Stevenson KJ. Influence of nitrogen doping on oxygen reduction electrocatalysis at carbon nanofiber electrodes. J Phys Chem B 2005;109:4707–16. doi:10.1021/jp044442z.

[17] Tang Y, Burkert SC, Zhao Y, Saidi WA, Star A. The Effect of Metal Catalyst on the Electrocatalytic Activity of Nitrogen-Doped Carbon Nanotubes. J Phys Chem C 2013;117:25213–21. doi:10.1021/jp403033x.

[18] Kundu S, Nagaiah TC, Xia W, Wang Y, Dommele S Van, Bitter JH, et al. Electrocatalytic Activity and Stability of Nitrogen-Containing Carbon Nanotubes in the Oxygen Reduction Reaction. J Phys Chem C 2009;113:14302–10. doi:10.1021/jp811320d.

[19] Singh D, Tian J, Mamtani K, King J, Miller JT, Ozkan US. A comparison of N-containing carbon nanostructures (CNx) and N-coordinated iron–carbon catalysts (FeNC) for the oxygen reduction reaction in acidic media. J Catal 2014;317:30–43. doi:10.1016/j.jcat.2014.05.025.

[20] Geng D, Liu H, Chen Y, Li R, Sun X, Ye S, et al. Non-noble metal oxygen reduction electrocatalysts based on carbon nanotubes with controlled nitrogen contents. J Power Sources 2011;196:1795–801. doi:10.1016/j.jpowsour.2010.09.084.

[21] Mo Z, Liao S, Zheng Y, Fu Z. Preparation of nitrogen-doped carbon nanotube arrays and their catalysis towards cathodic oxygen reduction in acidic and alkaline media. Carbon, 2012;50:2620–7. doi:10.1016/j.carbon.2012.02.021.

[22] Matter P, Zhang L, Ozkan U. The role of nanostructure in nitrogen-containing carbon catalysts for the oxygen reduction reaction. J Catal 2006;239:83–96. doi:10.1016/j.jcat.2006.01.022.

[23] Matter PH, Wang E, Arias M, Biddinger EJ, Ozkan US. Oxygen reduction reaction activity and surface properties of nanostructured nitrogen-containing carbon. J Mol Catal A Chem 2007;264:73–81. doi:10.1016/j.molcata.2006.09.008.

[24] Biddinger EJ, von Deak D, Ozkan US. Nitrogen-Containing Carbon Nanostructures as Oxygen-Reduction Catalysts. Top Catal 2009;52:1566–74. doi:10.1007/s11244-009-9289-y.

[25] Yin J, Qiu Y, Yu J, Zhou X, Wu W. Enhancement of electrocatalytic activity for oxygen reduction reaction in alkaline and acid media from electrospun nitrogen-doped carbon nanofibers by surface modification. RSC Adv 2013;3:15655. doi:10.1039/c3ra41389f.

[26] Sun Y, Wu Q, Shi G. Graphene based new energy materials. Energy Environ Sci 2011;4:1113. doi:10.1039/c0ee00683a.

[27] Higgins D, Zamani P, Yu A, Chen Z. The application of graphene and its composites in oxygen reduction electrocatalysis: a perspective and review of recent progress. Energy Environ Sci 2016. doi:10.1039/C5EE02474A.

[28] Li D, Müller MB, Gilje S, Kaner RB, Wallace GG. Processable aqueous dispersions of graphene nanosheets. Nat Nanotechnol 2008;3:101–5. doi:10.1038/nnano.2007.451.

[29] Zhao J, Guo Q, Shi J, Liu L, Jia J, Liu Y, et al. Carbon nanotube growth in the pores of expanded graphite by chemical vapor deposition. Carbon, 2009;47:1747–51. doi:10.1016/j.carbon.2009.02.028.

[30] Feng W, Qin M, Lv P, Li J, Feng Y. A three-dimensional nanostructure of graphite intercalated by carbon nanotubes with high cross-plane thermal conductivity and bending strength. Carbon, 2014;77:1054–64. doi:10.1016/j.carbon.2014.06.021.

[31] Schmidt TJ, Gasteiger HA, Stäb GD, Urban PM, Kolb DM, Behm RJ. Characterization of High-Surface-Area Electrocatalysts Using a Rotating Disk Electrode Configuration. J Electrochem Soc 1998;145:2354–8. doi:10.1149/1.1838642.

[32] Paulus UA, Schmidt TJ, Gasteiger HA, Behm RJ. Oxygen reduction on a high-surface area Pt/Vulcan

carbon catalyst: a thin-film rotating ring-disk electrode study. J Electroanal Chem 2001;495:134–45. doi:10.1016/S0022-0728(00)00407-1.

[33] Trasobares S, Stéphan O, Colliex C, Hsu WK, Kroto HW, Walton DRM. Compartmentalized CNx nanotubes: Chemistry, morphology, and growth. J Chem Phys 2002;116:8966. doi:10.1063/1.1473195.

[34] Chizari K, Sundararaj U. The effects of catalyst on the morphology and physicochemical properties of nitrogen-doped carbon nanotubes. Mater Lett 2014;116:289–92. doi:10.1016/j.matlet.2013.11.012.

[35] van Dommele S, Romero-Izquirdo A, Brydson R, de Jong KP, Bitter JH. Tuning nitrogen functionalities in catalytically grown nitrogen-containing carbon nanotubes. Carbon, 2008;46:138–48. doi:10.1016/j.carbon.2007.10.034.

[36] Rümmeli MH, Schäffel F, Bachmatiuk A, Adebimpe D, Trotter G, Börrnert F, et al. Investigating the outskirts of Fe and Co catalyst particles in alumina-supported catalytic CVD carbon nanotube growth. ACS Nano 2010;4:1146–52. doi:10.1021/nn9016108.

[37] He Z, Maurice J-L, Gohier A, Lee CS, Pribat D, Cojocaru CS. Iron Catalysts for the Growth of Carbon Nanofibers: Fe, Fe 3 C or Both? Chem Mater 2011;23:5379–87. doi:10.1021/cm202315j.

[38] Duan X, Qian G, Zhou X, Sui Z, Chen D, Yuan W. Tuning the size and shape of Fe nanoparticles on carbon nanofibers for catalytic ammonia decomposition. Appl Catal B Environ 2011;101:189–96. doi:10.1016/j.apcatb.2010.09.017.

[39] Dresselhaus MS, Jorio A, Hofmann M, Dresselhaus G, Saito R. Perspectives on carbon nanotubes and graphene Raman spectroscopy. Nano Lett 2010;10:751–8. doi:10.1021/nl904286r.

[40] Choi CH, Chung MW, Kwon HC, Chung JH, Woo SI. Nitrogen-doped graphene/carbon nanotube self-assembly for efficient oxygen reduction reaction in acid media. Appl Catal B Environ 2014;144:760–6. doi:10.1016/j.apcatb.2013.08.021.

[41] Arrigo R, Hävecker M, Wrabetz S, Blume R, Lerch M, McGregor J, et al. Tuning the acid/base properties of nanocarbons by functionalization via amination. J Am Chem Soc 2010;132:9616–30. doi:10.1021/ja910169v.

[42] Pels JR, Kapteijn F, Moulijn JA, Zhu Q, Thomas KM. Evolution of nitrogen functionalities in carbonaceous materials during pyrolysis. Carbon, 1995;33:1641–53. doi:10.1016/0008-6223(95)00154-6.

[43] Casanovas J, Ricart JM, Rubio J, Illas F, Jiménez-Mateos JM. Origin of the Large N 1s Binding Energy in X-ray Photoelectron Spectra of Calcined Carbonaceous Materials. J Am Chem Soc 1996;118:8071–6. doi:10.1021/ja960338m.

[44] Jaouen F, Herranz J, Lefèvre M, Dodelet J-P, Kramm UI, Herrmann I, et al. Cross-laboratory experimental study of non-noble-metal electrocatalysts for the oxygen reduction reaction. ACS Appl Mater Interfaces 2009;1:1623–39. doi:10.1021/am900219g.

[45] Artyushkova K, Kiefer B, Halevi B, Knop-Gericke A, Schlogl R, Atanassov P. Density functional theory calculations of XPS binding energy shift for nitrogen-containing graphene-like structures. Chem Commun 2013;49:2539. doi:10.1039/c3cc40324f.

[46] Matter P, Wang E, Ozkan U. Preparation of nanostructured nitrogen-containing carbon catalysts for the oxygen reduction reaction from SiO2- and MgO-supported metal particles. J Catal 2006;243:395–403. doi:10.1016/j.jcat.2006.07.029.

[47] Biddinger EJ, Deak D von, Singh D, Marsh H, Tan B, Knapke DS, et al. Examination of Catalyst Loading Effects on the Selectivity of CNx and Pt/VC ORR Catalysts Using RRDE. J Electrochem Soc 2011;158:B402. doi:10.1149/1.3552944.

[48] Merzougui B, Hachimi A, Akinpelu A, Bukola S, Shao M. A Pt-free catalyst for oxygen reduction reaction based on Fe–N multiwalled carbon nanotube composites. Electrochim Acta 2013;107:126–32. doi:10.1016/j.electacta.2013.06.016.

[49] Li X, Liu G, Popov BN. Activity and stability of non-precious metal catalysts for oxygen reduction in acid and alkaline electrolytes. J Power Sources 2010;195:6373–8. doi:10.1016/j.jpowsour.2010.04.019.

[50] Spendelow JS, Wieckowski A. Electrocatalysis of oxygen reduction and small alcohol oxidation in alkaline media. Phys Chem Chem Phys 2007;9:2654–75. doi:10.1039/b703315j.

[51] Ramaswamy N, Mukerjee S. Influence of Inner- and Outer-Sphere Electron Transfer Mechanisms during Electrocatalysis of Oxygen Reduction in Alkaline Media. J Phys Chem C 2011;115:18015–26. doi:10.1021/jp204680p.

[52] Ramaswamy N, Mukerjee S. Fundamental mechanistic understanding of electrocatalysis of oxygen reduction on Pt and non-Pt surfaces: Acid versus alkaline media. Adv Phys Chem 2012;2012. doi:10.1155/2012/491604.

[53] Dodelet J-P. The Controversial Role of the Metal in Fe- or Co-Based Electrocatalysts for the Oxygen Reduction Reaction in Acid Medium. In: Shao M, editor. Electrocatal. Fuel Cells A Non- Low- Platin. Approach, London: Springer-Verlag London; 2013, p. 271–338.

[54] Woods MP, Biddinger EJ, Matter PH, Mirkelamoglu B, Ozkan US. Correlation Between Oxygen Reduction Reaction and Oxidative Dehydrogenation Activities Over Nanostructured Carbon Catalysts. Catal Letters 2010;136:1–8. doi:10.1007/s10562-010-0304-5.

[55] Liu G, Li X, Ganesan P, Popov BN. Development of non-precious metal oxygen-reduction catalysts for PEM fuel cells based on N-doped ordered porous carbon. Appl Catal B Environ 2009;93:156–65. doi:10.1016/j.apcatb.2009.09.025.

[56] Liu G, Li X, Ganesan P, Popov BN. Studies of oxygen reduction reaction active sites and stability of nitrogen-modified carbon composite catalysts for PEM fuel cells. Electrochim Acta 2010;55:2853–8. doi:10.1016/j.electacta.2009.12.055.

[57] Kim H, Lee K, Woo SI, Jung Y. On the mechanism of enhanced oxygen reduction reaction in nitrogen-doped graphene nanoribbons. Phys Chem Chem Phys 2011;13:17505–10. doi:10.1039/c1cp21665a.

[58] Zhang P, Lian JS, Jiang Q. Potential dependent and structural selectivity of the oxygen reduction reaction on nitrogen-doped carbon nanotubes: a density functional theory study. Phys Chem Chem Phys 2012;14:11715. doi:10.1039/c2cp40087a.

[59] Wu G, More KL, Xu P, Wang H-L, Ferrandon M, Kropf AJ, et al. A carbon-nanotube-supported graphene-rich non-precious metal oxygen reduction catalyst with enhanced performance durability. Chem Commun 2013;49:3291–3. doi:10.1039/c3cc39121c.

[60] Liu G, Li X, Lee J-W, Popov BN. A review of the development of nitrogen-modified carbon-based catalysts for oxygen reduction at USC. Catal Sci Technol 2011;1:207. doi:10.1039/c0cy00053a.

[61] Herranz J, Jaouen F, Lefèvre M, Kramm UI, Proietti E, Dodelet J-P, et al. Unveiling N-protonation and anion-binding effects on Fe/N/C-catalysts for O2 reduction in PEM fuel cells. J Phys Chem C 2011;115:16087–97. doi:10.1021/jp2042526.